Contents lists available at ScienceDirect

Computers and Fluids

Interfacial deformation and jetting of a magnetic fluid

Shahriar Afkhami [a],[*], Linda J. Cummings [a], Ian M. Griffiths [b]

[a] Department of Mathematical Sciences, New Jersey Institute of Technology, Newark, NJ, USA
[b] Mathematical Institute, University of Oxford, Oxford, England, UK

ABSTRACT

An attractive technique for forming and collecting aggregates of magnetic material at a liquid–air interface by an applied magnetic field gradient was recently proposed, and its underlying principle was studied theoretically and experimentally (Tsai et al., 2013): when the magnetic field is weak, the deflection of the liquid–air interface has a steady shape, while for sufficiently strong fields, the interface destabilizes and forms a jet that extracts magnetic material. Motivated by this work, we develop a numerical model for the closely related problem of solving two-phase Navier–Stokes equations coupled with the static Maxwell equations. We computationally model the forces generated by a magnetic field gradient produced by a permanent magnet and so determine the interfacial deflection of a magnetic fluid (a pure ferrofluid system) and the transition into a jet. We analyze the shape of the liquid–air interface during the deformation stage and the critical magnet distance for which the static interface transitions into a jet. We draw conclusions on the ability of our numerical model to predict the large interfacial deformation and the consequent jetting, free of fitting parameters.

© 2015 Elsevier B.V. All rights reserved.

1. Introduction

Synthesis and assembly on the nanoscale is an important goal of contemporary science and technology. Magnetic nano/microparticles arise in a wide range of industrial and biomedical applications, and so are one target for controlled assembly. For example, functionalized magnetic microparticles can be used to separate cells [1] and magnetic microparticles have been used in microfluidics for cell sorting, blood cleansing, and magneto-capillary self-assembly (see e.g. [2] and references therein). When magnetic nanoparticles such as magnetite are suspended at high concentration in aqueous or non-aqueous carrier fluids, the entire system behaves as a continuum of magnetic fluid, known also as a ferrofluid. The rheology and interfacial shape of ferrofluids can be tuned with external magnetic fields, often in useful ways. An example is the application of ferrofluids in adaptive optics that has been considered in recent experiments [3,4]. The control of ferrofluid properties using magnetic fields also has applications in mechanical sealing and acoustics [5], targeted drug delivery [6–8] and treatment of retinal detachment [9].

Thin liquid films and droplets are ubiquitous in nature and also appear in many technological applications. The understanding of

their dynamical behavior and their stability is therefore of great importance and has attracted considerable attention in the literature. Recent research into thin film and droplet flows has resulted in many experimental and theoretical developments, including manipulating film flows via external magnetic or electric fields to produce nanoscale patterns. In particular, experiments on thin ferrofluid films and droplets have revealed the formation of a wide range of morphologies [10–14]. Ferrofluids can be manipulated using magnetic forces and have been extensively investigated and widely used in a variety of engineering applications; see Rosensweig [15] and a more recent review by Nguyen [16]. Normal field instability of ferrofluid films (and the equivalent electric field problem) have been extensively studied in the past, see e.g. [17,18]. However, despite the increase in the number of applications, surprisingly little can be found in the literature on the direct numerical simulations of thin ferrofluid films in the presence of a nonuniform magnetic field (such as is produced by a spherical magnet) and therefore our understanding of the instabilities that may occur in these flows is limited.

An attractive technique for forming and collecting aggregates of magnetic material at a liquid–air interface by an applied magnetic field was recently proposed, and its underlying principle was studied theoretically and experimentally, by Tsai et al. [19]. In the experiments described in [19], a water-based ferrofluid (EMG805, Ferrotec), with a density of 1200 kg m^{-3} and viscosity of 3 mPa s, is suspended in a shallow reservoir containing deionized water, with a density of 1000 kg m^{-3} and viscosity of 1 mPa s, to form

---

* Corresponding author.
E-mail address: shahriar.afkhami@njit.edu (S. Afkhami).

the magnetic mixture. This system is differentiated from a pure ferrofluid system because, in the presence of a magnet, it separates into a region rich with magnetic material, and one of negligible magnetic content. A spherical permanent magnet is slowly brought close to the magnetic mixture allowing the ferrofluid to aggregate and form a static hump at the liquid–air interface (see Fig. 1 in [19]). In these experiments, a distinct boundary that separates the magnetic and non-magnetic regions is observed. When the magnet is held sufficiently close to the liquid–air interface, the hump destabilizes and transforms to a jet. The theoretical approach developed in [19] describes a steady-state mathematical model for the behavior of the magnetic-particle-laden fluid and the particle-free fluid regions. The mathematical model results in [19] show excellent agreement with the experimental data.

Motivated by this work, here we develop a numerical model for a closely related problem: we computationally model the magnetically induced interfacial deflection of a magnetic fluid (ferrofluid) and the transition into a jet by a magnetic field gradient from a permanent magnet placed above the free surface. The system we study differs from that considered by Tsai et al. [19]: we consider a pure ferrofluid system, while Tsai et al. model a system with both magnetically dominated and non-magnetic regions. Fig. 1 shows a schematic illustrating the set-up we consider: the magnetic region occupied by pure ferrofluid, the liquid–air interface, and the spherical permanent magnet. The deformation of the ferrofluid–air interface arises as a result of the magnetic field gradient induced by the spherical permanent magnet held above the fluid; in line with the experiments we will see that, for sufficiently strong fields, the interface in our model destabilizes and forms a jet. We note that, although the focus of this work is to use a numerical study to uncover the transition to instability in a pure ferrofluid system, we believe that our study demonstrates some, perhaps not obvious, features of the development of the instability observed in the work of Tsai et al. [19]. The natural next step would be to consider the effect of the nonuniform distribution of the ferrofluid/magnetic particles, but this is beyond the scope of the present paper.

Here we solve the two-phase Navier–Stokes equations coupled with the static Maxwell equations in axisymmetric cylindrical polar

coordinates. We analyze the shape of the liquid–air interface during the deformation stage and the critical magnet distance (from the undeformed free surface), for which the static interface transitions into a jet. We draw conclusions regarding the ability of our numerical model to predict the large interfacial deformation and the consequent jetting, free of fitting parameters. The numerical model provides a realistic and accurate framework for predicting the evolution of magnetic liquids based on the Navier–Stokes equations.

We describe the details of the numerical model in Section 2. In Section 3, we describe a numerical boundary condition that may be implemented to simulate non-uniform magnetic fields. In Section 4, we present the numerical results and the comparison with experimental observations. In Section 5, we give an overview and future outlook for improving our modeling.

2. Mathematical model

Here we briefly describe the theoretical models that serve as a basis for the proposed numerical studies. The coupled motion of a ferrofluid surrounded by a non-magnetic fluid is governed by the (static) Maxwell equations, the Navier–Stokes equations, and a constitutive relationship for the magnetic induction $\mathbf{B}$, magnetic field $\mathbf{H}$, and the magnetization $\mathbf{M}$. The magnetostatic Maxwell equations for a non-conducting ferrofluid are, in SI units,

$$\nabla \cdot \mathbf{B} = 0, \quad \nabla \times \mathbf{H} = 0, \quad \mathbf{B}(\mathbf{x}, t) = \begin{cases} \mu_f \mathbf{H} & \text{in ferrofluid} \\ \mu_m \mathbf{H} & \text{in matrix,} \end{cases}$$

where μ_f denotes the magnetic permeability of the ferrofluid and μ_m is the permeability of the matrix fluid. For our application, the matrix fluid is air, which has a permeability very close to that for a vacuum, μ_o. Therefore, we shall consider $\mu_m = \mu_o$ throughout. A magnetic scalar potential ψ is defined by $\mathbf{H} = \nabla \psi$, and satisfies

$$\nabla \cdot (\mu \nabla \psi) = 0, \tag{1}$$

where $\mu = \mu_o$ and μ_f in the matrix and ferrofluid, respectively. We will assume that the magnetization is a linear function of the magnetic field given by $\mathbf{M} = \chi \mathbf{H}$, where $\chi = (\mu_f / \mu_o - 1)$ is the magnetic susceptibility [20]. The magnetic induction $\mathbf{B}$ is therefore $\mathbf{B} = \mu_o(\mathbf{H} + \mathbf{M}) = \mu_o(1 + \chi)\mathbf{H}$.

The fluid equation of motion is described by the conservation of mass and momentum (Navier–Stokes) equations

$$\nabla \cdot \mathbf{u} = 0, \tag{2}$$

$$\rho \left(\frac{\partial \mathbf{u}}{\partial t} + (\mathbf{u} \cdot \nabla)\mathbf{u} \right) = -\nabla p + \nabla \cdot (2\eta \mathbf{D}) + \nabla \cdot \tau_m + \mathbf{F}_s + \rho \mathbf{g}, \tag{3}$$

where $\mathbf{F}_s$ denotes the surface tension force per unit volume (presented as a body force [21]), p is pressure, $\mathbf{u}$ is velocity, $\mathbf{D} = \frac{1}{2}(\nabla \mathbf{u} + (\nabla \mathbf{u})^T)$ is the rate of deformation tensor (where T denotes the transpose), η is viscosity, ρ is density, τ_m is the magnetic stress tensor, and $\mathbf{g}$ is the gravitational acceleration. The total stress is $\tau = -p\mathbf{I} + 2\eta \mathbf{D} + \tau_m$, where $\mathbf{I}$ denotes the identity operator. The magnetic stress tensor of an incompressible, isothermal, magnetizable medium is [22]

$$\tau_m = -\frac{\mu_o}{2} H^2 \mathbf{I} + \mu \mathbf{H} \mathbf{H}^T,$$

where $H = |\mathbf{H}|$. These equations must be solved subject to suitable boundary and initial conditions, discussed in Section 3 below.

3. Numerical methodologies

We will use an Eulerian framework, where the material moves through a stationary mesh, and therefore a special procedure will

Fig. 1. A schematic illustrating the computational set-up and the coordinate system used. A spherical permanent magnet of radius R_m is centered at distance L from the initially undeformed film (red dashed line), which has a depth L_0. The magnetic force deforms the interface, $\partial \Omega_f$, into a hump (red solid line). A unit normal outwards from the interface is denoted by $\mathbf{n}$. A typical computational domain, Ω, and its boundary, $\partial \Omega$, is shown by the dash-dotted line. We use axisymmetric cylindrical polar coordinates. (For interpretation of the references to color in this figure legend, the reader is referred to the web version of this article.)

be required to track the interface between fluids. We will use the volume of fluid (VOF) method to track the interface between the ferrofluid and the matrix fluid [23–25]. In this way, the VOF formulation describes each fluid by assigning a volume fraction function, $f(r, z, t)$, as

$$f(r, z, t) = \begin{cases} 1 & \text{in ferrofluid} \\ 0 & \text{in matrix} \end{cases} \tag{4}$$

(see Fig. 1 for the polar coordinates (r, z) used here). The position of the interface is computed from $f(r, z, t)$ by reconstructing the curve where the step discontinuity takes place. In this work, the reconstruction is a 'piecewise linear interface calculation' (PLIC) [26]. To track the interface, $f(r, z, t)$ is advected by the flow,

$$\frac{\partial f}{\partial t} + \nabla \cdot (\mathbf{u} f) = 0. \tag{5}$$

In the Navier–Stokes equations (Eq. (3)), $\mathbf{F}_s$ includes the continuum body force due to interfacial tension

$$\mathbf{F}_s = \sigma \kappa \delta_S \mathbf{n}, \tag{6}$$

where σ denotes the surface tension, κ the curvature of the interface, the unit normal $\mathbf{n} = \nabla f / |\nabla f|$, and $\delta_S = |\nabla f|$ is the delta function at the interface.

3.1. An effective method for simulating non-uniform magnetic fields

Special care must be taken when computing the solution of the Maxwell equations to account, accurately and robustly, for the non-uniformity of the magnetic field. The boundary condition on the magnetic field is reconstructed from an exact solution of the magnetic field due to a spherical magnet, in the absence of the ferrofluid. We let ψ_a denote the magnetic potential for this infinite-domain analytical solution, satisfying Laplace's equation, in cylindrical coordinates with azimuthal symmetry,

$$\frac{1}{r} \frac{\partial}{\partial r} \left(r \frac{\partial \psi_a}{\partial r} \right) + \frac{\partial^2 \psi_a}{\partial z^2} = 0.$$

We assume a magnetic potential generated by a uniformly magnetized spherical magnet, as in [19], hence

$$\psi_a(r, z) = \left\{ \frac{M_m R_m^3 (L - (z - L_0)) r}{3 \left[(L - (z - L_0))^2 + r^2 \right]^{3/2}} \right\} + \text{constant}, \tag{7}$$

where M_m is the magnetization of the magnet and R_m is the radius of the magnet. The magnet center is at $(r, z) = (0, L + L_0)$, where L is the magnet distance from the undeformed interface and L_0 is the initial unperturbed interfacial depth in our problem set-up (see Fig. 1). The analytical magnetic field $\mathbf{H}_a = \nabla \psi_a$ is thus

$$\mathbf{H}_a = \left\{ \frac{M_m R_m^3 ((z - L_0) - L) r}{\left[(L - (z - L_0))^2 + r^2 \right]^{5/2}} \right\} \hat{\mathbf{r}}$$
$$+ \left\{ \frac{M_m R_m^3 \left[2((z - L_0) - L)^2 - r^2 \right]}{3 \left[(L - (z - L_0))^2 + r^2 \right]^{5/2}} \right\} \hat{\mathbf{z}}, \tag{8}$$

where $\hat{\mathbf{r}}$ and $\hat{\mathbf{z}}$ denote the unit vectors in the r and z directions, respectively. This solution will provide the boundary condition for the magnetic field generated by the permanent magnet, as we now explain.

The numerical magnetic potential ψ is calculated by solving Eq. (1) on the computational domain Ω (see Fig. 1) using a multi-grid algorithm, as described in [20], with appropriate boundary conditions. We note that in all simulations presented below, the

spherical magnet lies outside the computational domain. The numerical solution to the elliptic partial differential equation for ψ (Eq. (1)) will be complicated by the fact that the magnetic permeability, μ, experiences a jump across the interface [20]. The boundary conditions for ψ on the domain boundaries $\partial \Omega$ are defined as

$$\frac{\partial \psi}{\partial n} = \frac{\partial \psi_a}{\partial n} \quad \text{on } \partial \Omega, \tag{9}$$

where $\partial / \partial n = \mathbf{n}_\Gamma \cdot \nabla$, and $\mathbf{n}_\Gamma$ denotes the normal to the boundary $\partial \Omega$. In order to impose the boundary condition in our numerical model, we perform a transformation of variables to $\zeta : \psi = \psi_a + \zeta$, where ψ_a is the potential field without the magnetic medium, Eq. (7). One can then rewrite Eq. (1) such that

$$\nabla \cdot (\mu \nabla \zeta) = -\nabla \cdot (\mu \nabla \psi_a), \tag{10}$$

where $\nabla \cdot (\mu \nabla \psi_a)$ vanishes everywhere except on the surface between the ferrofluid/matrix interface $\partial \Omega_f$ and

$$\frac{\partial \zeta}{\partial n} = 0 \quad \text{on } \partial \Omega. \tag{11}$$

Though we do not use this in the following analysis, we note that our numerical approach may also be used to model the nonlinear magnetic susceptibility of ferrofluids; for example, the well-known Langevin function $L(\alpha) = \coth \alpha - \alpha^{-1}$ can be implemented to describe the magnetization behavior of the ferrofluid versus the strength of the magnetic field $\mathbf{H}$,

$$\mathbf{M(H)} = M_s L \left(\frac{\mu_o m |\mathbf{H}|}{k_B T} \right) \frac{\mathbf{H}}{|\mathbf{H}|}, \tag{12}$$

where the saturation magnetization M_s and the magnetic moment of the particle enter as parameters, T denotes the absolute temperature, and k_B is the Boltzmann constant.

3.2. Pressure, velocity, and volume fraction boundary conditions

We impose symmetry boundary conditions at the axis $r = 0$. At the top $(z = L_z)$, bottom $(z = 0)$ and right $(r = L_r)$ boundaries, we impose solid-wall boundary conditions for the pressure and the velocities. The boundary condition for the volume fraction function at the top wall is $f = 0$, at the bottom wall is $f = 1$, and for the right (outer) wall is that the interface has zero slope: $\partial f / \partial r = 0$ on $r = L_r$. We have also varied the computational domain in simulations to verify that it is large enough for the boundary to have negligible effect on the deformation of the liquid–air interface.

4. Results and discussion

Numerical simulations are presented in three parts. First we present tests of the numerical implementation by focusing on the resulting magnetic fields and by studying the convergence of the solution for the magnetic field with grid refinement. Second, we present several numerical solutions of our system that demonstrate both the steady-interfacial-deflection regime, and the transition from this regime to the unstable jetting regime. Third, we examine the effect of varying the magnetic Bond number, which characterizes the dominant balance between the magnetic and surface tension forces, in the steady-interfacial-deflection regime.

Our numerical set-up closely follows that in [19]; a spherical permanent magnet of radius R_m and magnetization $M_m = 10^6$ A m^{-1} is placed at a distance L from the initially undeformed ferrofluid film (see Fig. 1). The ferrofluid has a density $\rho_f = 1200$ kg m^{-3}, viscosity $\eta_f = 3$ mPa s, and surface tension $\sigma = 0.07$ N m^{-1}. The ferrofluid is assumed to have a constant magnetic susceptibility, χ, which will be determined by comparing the numerical result with the experimental data in [19] (note that this

value is often not reported by manufacturers so is determined by users).

4.1. Magnetic field and imposed numerical boundary condition

We first demonstrate the effectiveness of our methodology for computing the magnetic field by presenting the results of the simulated applied magnetic field using the numerical boundary conditions described in Section 3.1. The following relative error norms are defined

$$L_2(H, \Delta) = \frac{||H||_{2,\Delta} - ||H||_{2,\Delta_{max}}}{||H||_{2,\Delta_{max}}}, \quad L_\infty(H, \Delta) = \frac{||H||_{\infty,\Delta} - ||H||_{\infty,\Delta_{max}}}{||H||_{\infty,\Delta_{max}}},$$

where

$$||H||_{2,\Delta} = \sqrt{\Sigma_i \Sigma_j H_{ij}^2 \Delta^2} \quad \text{and} \quad ||H||_{\infty,\Delta} = \text{Max}\big(|H_{ij}|\big)_\Delta,$$

where i and j are indices of a computational cell. Fig. 2 shows the computational domain $\Omega : r \in (0, L_r)$ and $z \in (0, L_z)$, where $(L_r, L_z) = (1.5\text{ mm}, 3\text{ mm})$, with a 1 mm radius permanent magnet placed 5 mm above the r-axis. The mesh size $\Delta = L_r/N_r = L_z/N_z$, where N_r and N_z are the number of grid points in r and z directions, respectively. The computed magnetic field strength, H, is also shown in Fig. 2.

Fig. 3 exhibits the convergence of the numerical method with spatial resolution for computing the magnetic field. As illustrated, a second-order convergence is obtained for the mesh refinement for both L_2 and L_∞ error measures. The figure also reveals the smallness of the errors even at a coarse grid resolution. Finally the accuracy of the numerical solution is also assessed by comparing the computed magnetic field with the exact solution for a
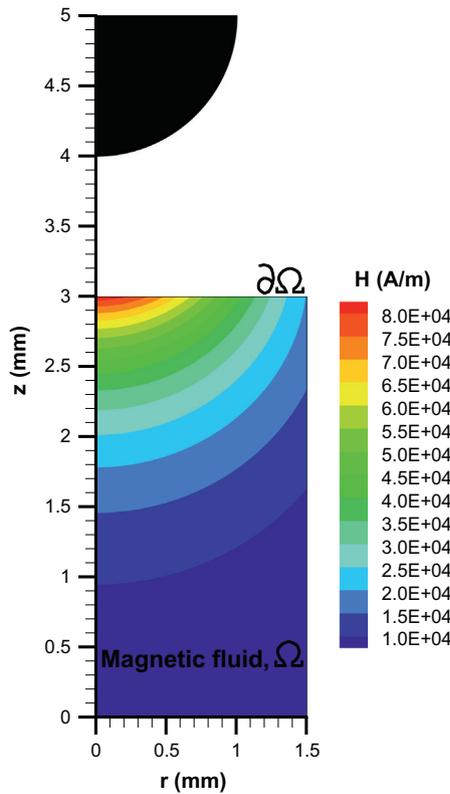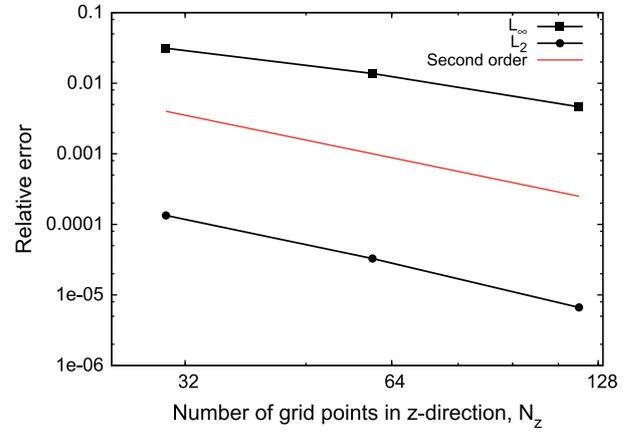
Fig. 3. The convergence of the L_2 and L_∞ relative error norms between the $H(r, z)$ computed at $\Delta = L_z/N_z (= L_r/N_r)$ and at $\Delta_{max} = L_z/240$, for the computational set-up illustrated in Fig. 2.

spherical magnet in an unbounded region given by Eq. (8); the maximum errors in H are of the order 0.01%. These results confirm the overall consistency and accuracy of the computational scheme with the implemented numerical boundary conditions as described in Section 3.1.

4.2. Interfacial deflection and transition to jetting

Tsai et al. describe the results of experiments and mathematical analysis of the deformation of a free surface by a magnetic force from a spherical permanent magnet [19]. As mentioned earlier, in that work the system consists of both magnetic and non-magnetic regions such that the magnetic particles collect at the interface, causing deformation of the free surface to form a hump; and when the magnet is brought sufficiently close, the hump transitions to a jet. The system we investigate computationally here differs from that of [19] because our liquid region contains a homogeneous ferrofluid. The study we present next therefore is not an attempt to provide quantitative comparisons with the experiments of Tsai et al., but an effort, for the first time, to reveal the essential features of experimental results by directly solving the governing equations of a model system. Despite the differences between our model and the experimental set-up, here we also observe the same qualitative features as in the experiments of Tsai et al.: when the magnet is positioned sufficiently far from the ferrofluid, the deformation of the interface is static; and when we reduce the distance between the magnet and the undeformed interface, the deformation destabilizes into jet formation. We also note that our model is able to validate and build on the scaling-law prediction for the jetting transition presented in [19] by predicting the transition point free of any fitting parameter.

In Fig. 4 , we present the results of direct computations of our system in the static-deformation regime. In these simulations, the computational domain is $L_r = 15$ mm by $L_z = 2.5$ mm and the undeformed film is initially located at $L_0 = 1$ mm. A magnet of radius $R_m = 3.2$ mm is placed at distance $L = 6.33$ mm (Fig. 4(a)) and 5.65 mm (Fig. 4(b)) from the undisturbed film. In Fig. 4, we also reproduce the experimental results of [19] to compare and contrast the two systems.

We note that in practice it is very difficult to control or measure the magnetic susceptibility of a ferrofluid sample accurately. We therefore use the comparison of the computed steady-state hump height, h, with the experimental measurement to determine the magnetic susceptibility of the ferrofluid. This comparison gives

Fig. 2. The computational domain, Ω, and the computed magnetic field strength, H, with a drawing of a permanent magnet overlaid. The spherical magnet lies outside the computational domain. Number of grid points in the z-direction is $N_z = 240$ and in the r-direction is $N_r = 120$.
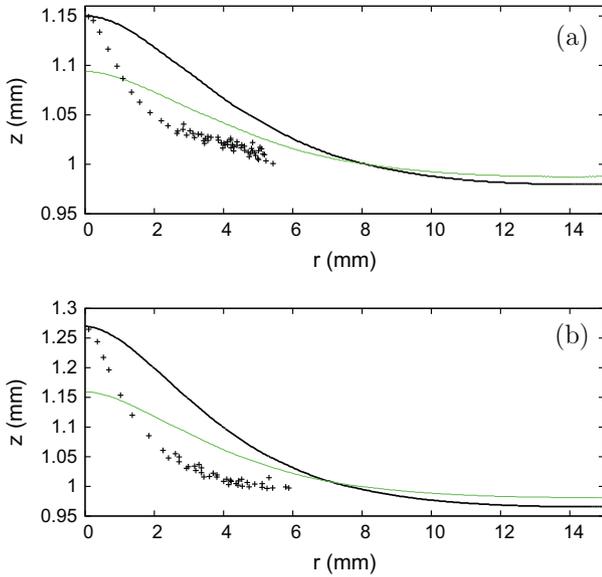
Fig. 4. Experimental data (not pure ferrofluid) from [19] shown alongside our computed steady-state ferrofluid–air interfacial profiles for (a) $L = 6.33$ mm and (b) $L = 5.65$ mm. Black solid lines have $\chi = 7.5 \times 10^{-4}$, chosen to match maximum free surface height to data; green solid lines have $\chi = 5 \times 10^{-4}$, chosen to fit the data as a whole. The results illustrate the height of the hump and the radial spread of the ferrofluid–air interface. (For interpretation of the references to color in this figure legend, the reader is referred to the web version of this article.)

$\chi = 7.5 \times 10^{-4}$, a value consistent with the finding in [19]. In Fig. 4, we also demonstrate the results when using $\chi = 5 \times 10^{-4}$, a value chosen to fit the data as a whole rather than just fitting to the maximum hump height. Although the results demonstrate consistency between the direct numerical solutions and the experiments in capturing the height of the hump, the agreement in the profile is not quantitative, owing to fact that the experimental system is not pure ferrofluid. Our study can therefore be interpreted as a way of determining the effective susceptibility of a material by, in some way, comparing our numerical results with the experiments. We note that even though neither of the parameter fits in Fig. 4 are able to reproduce both the maximum height and the overall shape that are observed in the experiment, the corresponding values for the susceptibility are consistent with those found in [19].

With this caveat in mind, we next investigate the transition to jetting with $\chi = 7.5 \times 10^{-4}$. In Fig. 5, we show a series of static ferrofluid–air interface profiles as the distance L between magnet center and undeformed ferrofluid interface is reduced. As the magnet separation L is decreased incrementally, we find that there exists a
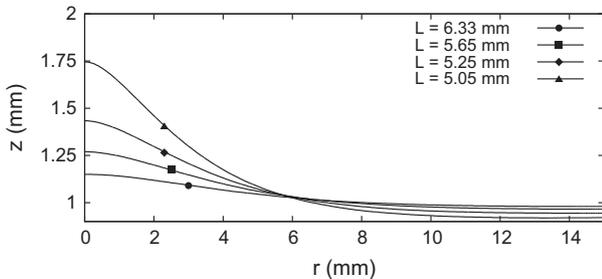
Fig. 5. Static ferrofluid–air interfaces when varying L; for $L \lesssim 5.05$ mm, no static hump can form. A decrease in L results in decreasing the radial spreading. The hump also becomes less pronounced with increasing L.

threshold for the jetting transition: for $L \lesssim 5.05$ mm, we no longer see the free surface evolving to a static configuration; instead, the ferrofluid–air interface destabilizes and forms a jet. The maximum sustainable steady interfacial deflection that we were able to compute occurs at $L = 5.05$ mm, consistent with the experimental finding in [19]. Also consistent with the experimental observations, we find that the steady interfacial deflection increases and the radial spreading decreases, with decreasing L, until the hump transitions to jetting. We attribute this qualitative agreement to the fact that our set-up, while not identical to the experimental set-up in [19], still possesses the main physical features that control the instability threshold: mainly, the characteristic interfacial deflection can be related to the dominant balance between the paramagnetic attraction and the surface tension.

In Fig. 6, we plot interface evolution when the magnet is sufficiently far away ($L = 5.25$ mm) that the interface reaches a static state (Fig. 6(a)); and when it is close enough ($L = 4.95$ mm) that jetting occurs (Fig. 6(b)), where no sustainable static interfacial deflection can be obtained. Interestingly, for $L = 5.25$ mm (Fig. 6(a)), we find an overshoot in deformation; i.e., an initial elongation followed by a retraction to a static state. We attribute the overshoot mainly to the dominant competition between magnetic, capillary, and inertial effects. However, we have not explored the effect of varying the gravitational acceleration, which might also contribute to this behavior, and leave this for a future study. Also, as illustrated, for $L = 4.95$ mm (Fig. 6(b)), the interface becomes unstable and stretches until it touches the top boundary of the computational domain while for $L = 5.25$ mm, a stable interface is achieved. We also note that, when the interface destabilizes, the deflection increases very rapidly as the ferrofluid–air interface approaches the magnet.

We also investigate the effect of increasing the magnetic susceptibility and the magnet size. In Fig. 7(a), we plot the ferrofluid–air interface for $\chi = 1.75$ as a function of time for $L = 6.75$ mm and $R_m = 1.5$ mm. We also plot the case when $\chi = 0.75$ in Fig. 7(b). These results indicate that increasing the magnetic susceptibility can destabilize a previously stable interface, moving it into the jetting regime; and that when the magnet size is reduced, a much higher magnetic susceptibility is required to destabilize the interface into jetting. These predictions can be used to find the optimal magnet size for destabilizing the interface based on the susceptibility of the magnetic fluid. For a fixed magnet distance L and magnet size R_m, transition to jetting occurs for a certain value of the magnetic susceptibility χ. When the magnet is brought slightly closer (decreasing L), the transition occurs for a smaller χ value. Fig. 8 shows the results for increasing the magnetic susceptibility, which leads to an increase in the interfacial deflection for $L = 6$ mm and $R_m = 1.5$ mm. This figure shows that, for a sufficiently high magnetic susceptibility, the surface tension of the ferrofluid can no longer sustain the deformation and jetting again occurs. We find that in this case, for $\chi \gtrsim 0.1$, no static hump can form. We also note that for $\chi = 0.75$ in Fig. 8, a secondary instability appears to form at the tip of the jet, although this instability will not have sufficient time to grow (most likely into a pinch-off structure) before the tip touches the magnet.

4.3. Scaling model for interfacial deflection

Finally, we investigate the maximum interfacial deformation, $h(0)$, defined as the maximum height of the hump at $r = 0$, as L varies. To characterize this behavior, it is helpful to represent the results in terms of the following dimensionless parameters [19]: the magnetic Bond number

$$\text{Bo}_m = \frac{\chi \mu_o M_m^2 R_m}{\sigma},$$
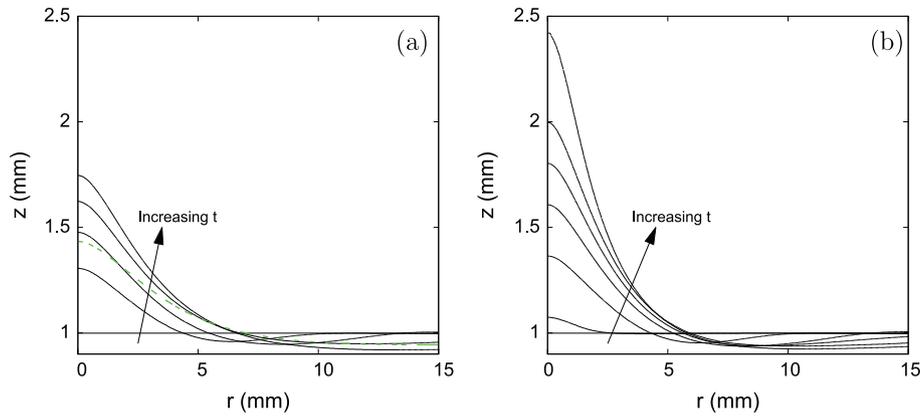
Fig. 6. The ferrofluid–air interface. (a) $t = 0, 25, 50, 100, 200, 450$ ms (from bottom to top) for $L = 5.25$ mm. The interface deforms and reaches a static state (green dashed line); the interface undergoes a transient overshoot before settling down to a static shape. The arrow marked "Increasing t" refers only to the solid (black) curves. (b) $t = 0, 5, 25, 50, 100, 150, 200, 248$ ms (from bottom to top) for $L = 4.95$ mm. No sustainable steady interfacial deflection can be obtained and the dynamic interface grows until it touches the top boundary of the computational domain at 250 ms (not shown here). The magnet radius $R_m = 3.2$ mm and the experimentally fitted value of the magnetic susceptibility $\chi = 7.5 \times 10^{-4}$. (For interpretation of the references to color in this figure legend, the reader is referred to the web version of this article.)
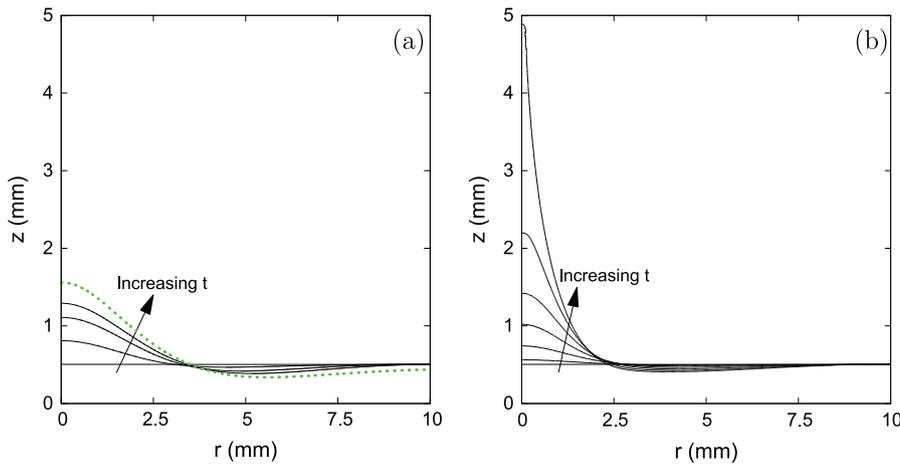
Fig. 7. The ferrofluid–air interface. (a) $t = 0, 12.5, 25, 37.5$ ms (from bottom to top) for $\chi = 0.75$. The interface deforms and reaches a static state (green dashed line) at around $t = 150$ ms. (b) $t = 0, 2.5, 5, 7.5, 10, 12.5, 15$ ms (from bottom to top) for $\chi = 1.75$. The interface touches the top boundary of the computational domain at around 16 ms (not shown here). $L = 6.75$ mm and $R_m = 1.5$ mm. The flat interface shows the initial position of the ferrofluid–air interface. (For interpretation of the references to color in this figure legend, the reader is referred to the web version of this article.)
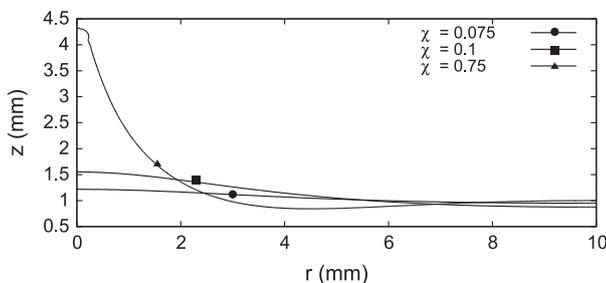
Fig. 8. The ferrofluid–air interface when varying χ; for $\chi \gtrsim 0.1$, no static hump can form. Increasing χ results in transition to jetting. For $\chi = 0.75$, the dynamic interface stretches until it touches the top boundary of the computational domain, while the interface reaches a static state for $\chi = 0.075$ and $\chi = 0.1$. In all cases $L = 6$ mm and $R_m = 1.5$ mm. A secondary instability (or necking that will grow into a pinch-off structure) appears to develop at the tip of the jet for $\chi = 0.75$.

which represents the ratio of the magnetic to surface tension force; and

$$L^* = \frac{L}{R_m} \quad \text{and} \quad h^* = \frac{h}{R_m},$$

which give the dimensionless distance between the magnet center and the initially undeformed ferrofluid film, and the dimensionless height of the hump, respectively. In Fig. 9, we present the results of the maximum dimensionless interfacial deformation, $h^*(0)$, predicted by our computational model, versus dimensionless magnet distance L^*, for several values of Bo$_m$. Again, we see that as the magnet is successively brought closer to the interface, the maximum hump height increases. We also present the effect of the magnetic Bond number, showing an increase in the maximum interfacial deformation as the magnetic Bond number is increased. For all values of Bo$_m$ considered, the results show that the maximum interfacial deflection does not vary significantly prior to jetting, while the magnitude of the maximum deflection increases rapidly for smaller L^*. Past the critical values of L^*, no static profile can be obtained (the critical points are shown by red arrows in Fig. 9). In general, the results indicate that when using a ferrofluid with a smaller susceptibility, the magnet must be placed closer to the interface to produce jetting.

Analogous to the study in [19], we identify the natural scaling for the characteristic interfacial deflection h_c by
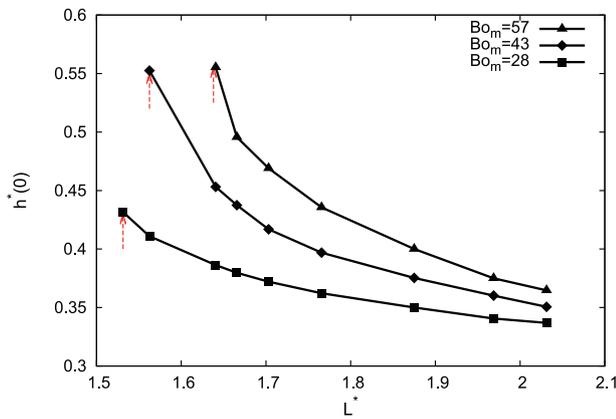
Fig. 9. The maximum interfacial deformation, $h^*(0)$, versus the non-dimensional distance between the magnet center and the initially flat film, L^*, for various magnetic Bond numbers, Bo_m. $R_m = 3.2$ mm and $\sigma = 0.07$ N m^{-1}. Critical points are marked by red arrows; a smaller L^* will result in no static profiles. (For interpretation of the references to color in this figure legend, the reader is referred to the web version of this article.)
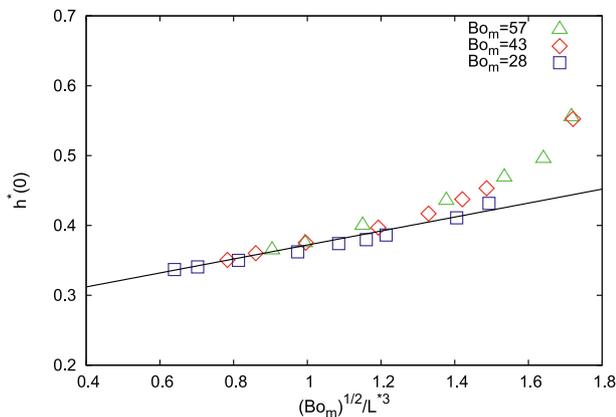
Fig. 10. Non-dimensional maximum interfacial deformation, $h^*(0)$, plotted against $(Bo_m)^{1/2}/L^{*3}$ for the results in Fig. 9. The solid line is the scaling fit, $h^*(0) \propto (Bo_m)^{1/2}/L^{*3}$.

$$h_c^2 = \frac{\mu_o \chi M_m^2 R_m^9}{\sigma L^6} = \frac{Bo_m R_m^8}{L^6}, \qquad (13)$$

representing the dominant balance between the magnetic and surface tension forces. Numerical results in Fig. 9 suggest that, prior to jetting, the maximum interfacial deflections do not vary significantly for different values of Bo_m. Motivated by this observation, we use Eq. (13) to determine the scaling relationship between the maximum interfacial deflection and the parameters that we vary in our numerical simulations: L^* and Bo_m. In Fig. 10, we plot $h^*(0)$ versus $\sqrt{Bo_m}/L^{*3}$, predicted by the scaling model Eq. (13). Further from the transition, the simulations results collapse remarkably well onto this single scaling relationship. Close to the jetting, however, we observe a deviation from the scaling law, whereby the assumption of slowly varying $h^*(0)$ versus L^* breaks down.

5. Conclusions

In this paper, we have carried out direct computations of the deformation of a ferrofluid–air interface under an external magnetic field gradient generated by a spherical magnet placed at a fixed distance from the interface. We showed that, when the magnet is sufficiently far from the interface, the free surface deformation is static,

while below a threshold value, the interface destabilizes and forms a jetting fluid. These features are also observed experimentally, in a different but related system in which the ferrofluid is suspended in water [19]. Our numerical results provide data that can be used to determine the maximum deflection of a ferrofluid in the presence of a magnetic field gradient generated by an external permanent magnet and the consequent transition to jetting. Additionally, a simple scaling law allows us to collapse our numerical results from a series of configurations onto a single power law. It is interesting to note that, while the key features observed in the experiments are reproduced in our pure ferrofluid simulations (i.e., static interfacial deformations at large magnet separation or low magnetic susceptibility, with transition to jetting at small magnet separations or high magnetic susceptibility), the static interfacial profiles obtained in the two systems are rather different. In particular, the interfacial profiles for the water–ferrofluid mix are more "peaked" under the same conditions than those for pure ferrofluid; see Fig. 4. This could be due to the water providing a lubricating "slip" layer that allows the ferrofluid to be more mobile in the experiments. Investigating such mixed systems computationally will be deferred to a future publication.

References

[1] Moldday R, Rembaun SYA. Application of magnetic microspheres in labelling and separation of cells. Nature 1977;268:437–8.
[2] Tsai SSH, Wexler JA, Wan J, Stone HA. Microfluidic ultralow interfacial tensiometry with magnetic particles. Lab Chip 2013;13:119–25.
[3] Malouin BA, Vogel MJ, Hirsa AH. Electromagnetic control of coupled droplets. Appl Phys Lett 2010;96.
[4] Malouin BA, Vogel MJ, Olles JD, Cheng L, Hirsa AH. Electromagnetic liquid pistons for capillarity-based pumping. Lab Chip 2011;11:393–7.
[5] Raj K, Moskowitz B, Casciari R. Advances in ferrofluid technology. J Magn Magn Mater 1995;149:174–80.
[6] Yue P, Lee S, Afkhami S, Renardy Y. On the motion of superparamagnetic particles in magnetic drug targeting. Acta Mech 2012;223:505–27.
[7] Cherry EM, Eaton JK. A comprehensive model of magnetic particle motion during magnetic drug targeting. Int J Multiphase Flow 2014;59:173–85.
[8] Grant H, Scardovelli R, Trubatch AD, Yecko PA. Height function based volume of fluid code for simulations of multiphase magnetic fluids. Comput Fluids 2015;113:112–18.
[9] Mefford OT, Woodward RC, Goff JD, Vadala TP, St Pierre TG, Dailey JP, et al. Field-induced motion of ferrofluids through immiscible viscous media: Testbed for restorative treatment of retinal detachment. J Magn Magn Mater 2007;311:347–53.
[10] Baygents JC, Rivette NJ, Stone HA. Electrohydrodynamic deformation and interaction of drop pairs. J Fluid Mech 1998;368:359–75.
[11] Stone HA, Lister JR, Brenner MP. Drops with conical ends in electric and magnetic fields. Proc R Soc Lond A 1999;455:329–47.
[12] Chen C-Y, Cheng Z-Y. An experimental study on Rosensweig instability of a ferrofluid droplet. Phys Fluids 2008;20:054105.
[13] Chen C-Y, Li C-S. Ordered microdroplet formations of thin ferrofluid layer breakups. Phys Fluids 2010;22:014105.
[14] Dickstein A, Erramilli S, Goldstein R, Jackson D, Langer S. Labyrinthine pattern formation in magnetic fluids. Science 1993;261:1012–15.
[15] Rosensweig RE. Magnetic fluids. Annu Rev Fluid Mech 1987;19:437–63.
[16] Nguyen N. Micro-magnetofluidics: interactions between magnetism and fluid flow on the microscale. Microfluid Nanofluid 2012;12:1–16.
[17] Craster RV, Matar OK. Electrically induced pattern formation in thin leaky dielectric films. Phys Fluids 2005;17:032104.
[18] Seric I, Afkhami S, Kondic L. Interfacial instability of thin ferrofluid films under a magnetic field. J Fluid Mech Rapids 755 ⟨10:underline⟩http://dx.doi.org/10.1017/jfm.2014.435⟨/10:underline⟩.
[19] Tsai SSH, Griffiths IM, Li Z, Kim P, Stone HA. Interfacial deflection and jetting of a paramagnetic particle-laden fluid: theory and experiment. Soft Matter 2013;9:8600–8.

[20] Afkhami S, Tyler A, Renardy Y, Renardy M, St Pierre TG, Woodward R, et al. Deformation of a hydrophobic ferrofluid droplet suspended in a viscous medium under uniform magnetic fields. J Fluid Mech 2010;663:358–84.

[21] Brackbill JU, Kothe DB, Zemach C. A continuum method for modeling surface tension. J Comput Phys 1992;100:335–54.

[22] Rosensweig RE. Ferrohydrodynamics. New York: Cambridge University Press; 1985.

[23] Francois MM, Cummins SJ, Dendy ED, Kothe DB, Sicilian JM, Williams MW. A balanced-force algorithm for continuous and sharp interfacial surface tension models within a volume tracking framework. J Comput Phys 2006;213:141–73.

[24] Afkhami S, Bussmann M. Height functions for applying contact angles to 2D VOF simulations. Int J Numer Meth Fluids 2008;57:453–72.

[25] Afkhami S, Bussmann M. Height functions for applying contact angles to 3D VOF simulations. Int J Numer Meth Fluids 2009;61:827–47.

[26] Li J, Renardy Y. Direct simulation of unsteady axisymmetric core-annular flow with high viscosity ratio. J Fluid Mech 1999;391:123–49.